$$Q' = Q_0[1 - \sin^2(\Psi)\sin^2(\theta)]^{1/2} \quad (1)$$

$$Q' \cos(\Psi') = Q_0 \cos(\Psi) \quad (2)$$

In Fig. 4, C and D, the two sets of optical diffraction spots, from Figs. 3A and 3B, respectively, are shown fit to ellipses given by Eqs. 1 and 2. The open circles are the experimental points. Because, in each data set, the magnitude of the scattering vectors for the spots with the largest spacing were approximately $2\pi/d = 1.53$ nm^{-1}, these spots were taken to define the Q_a axis. The points in Fig. 4C closest to the Q'_b axis correspond to diffraction from blocks similar in orientation to the rightmost blocks in Fig. 4A. The intersection of the fracture surface with these blocks results in only a few layer "lines," and the resulting diffraction features were either diffuse (Fig. 3A) or unobservable (Fig. 3B). The ×'s in Fig. 4, C and D, are the expected locations of the optical diffraction spots for a constant rotation angle between layer blocks of $\Delta\Psi$. Except for the single point in Fig. 4C near the Q'_b axis (which corresponds to one of the weakest diffraction features), excellent agreement between the fits and the data are obtained for $\theta = 60°$ and $\Delta\Psi = 15.5°$ for Fig. 4C and $\theta = 55°$ and $\Delta\Psi = 19°$ for Fig. 4D. This variation in $\Delta\Psi$ is within the range consistent with the temperature variation of the helical pitch. Of course, the real fracture surface is not planar, but this idealized fracture closely approximates the optical diffraction. [The symmetry of the optical transforms in Fig. 3 is broken by the shadowing effect of the sample preparation (27), and hence only two of the four quadrants of the ideal transform are visible.] Finally, the parameters that give the best fit in Fig. 4C have approximately the same values as the parameters used in generating Fig. 4A.

From the average $\Delta\Psi$ and the measured layer spacing of 4.1 nm, we calculate a spacing between screw dislocations, $\ell_d \approx d/\Delta\Psi = 14$ to 15 nm, which is consistent with our observations of the screw dislocation density in Fig. 2B. From our measured $\Delta\Psi$ and the measured pitch, $\lambda_0 \approx 0.5$ to 0.6 μm, we estimate the distance between grain boundaries, $\ell_b \approx \lambda_0\Delta\Psi/2\pi = 24$ to 28 nm.

Our freeze-fracture results give clear evidence that the TGB model is a good description of the SmA* phase. The images show a regular undulating cholesteric-like structure with a length scale of 0.5 to 0.6 μm, consistent with a macroscopic helical pitch, and simultaneously show the smectic layering with a spacing of 4.1 nm. In addition, we see the characteristic fracture pattern of a high density of elementary screw dislocations oriented normal to the twist axis. Optical diffraction shows that the layers twist in discrete steps of about 17°, dictating that the screw dislocations are spaced every 14 to 15 nm and there is about 24 nm between grain boundaries. This combination of evidence, which is unobtainable by any other technique, clearly shows that the SmA* phase is the liquid-crystal analog of the Abrikosov phase in superconductors and completes the analogy between smectic phases and superconductors as given by the TGB model.

REFERENCES AND NOTES

1. J. W. Goodby *et al.*, *Nature* **337**, 449 (1989).
2. J. W. Goodby *et al.*, *J. Am. Chem. Soc.* **111**, 8119 (1989).
3. A. J. Slaney and J. W. Goodby, *J. Mater. Chem.* **1**, 5 (1991).
4. F. C. Frank, *Disc. Faraday Soc.* **25**, 19 (1958).
5. S. R. Renn and T. C. Lubensky, *Phys. Rev. A* **38**, 2132 (1988).
6. P. G. de Gennes, *Solid State Commun.* **10**, 753 (1972).
7. ______, *Science* **256**, 495 (1992).
8. A. A. Abrikosov, *Sov. Phys. JETP* **5**, 1174 (1957).
9. G. Srajer, R. Pindak, M. A. Waugh, J. W. Goodby, J. S. Patel, *Phys. Rev. Lett.* **64**, 1545 (1990).
10. J. M. Carlson and J. P. Sethna, *Phys. Rev. A* **36**, 3359 (1987).
11. J. A. N. Zasadzinski, J. Schneir, J. Gurley, V. Elings, P. K. Hansma, *Science* **239**, 1013 (1988).
12. J. Garnaes, D. K. Schwartz, R. Viswanathan, J. A. N. Zasadzinski, *Nature* **357**, 54 (1992).
13. D. Schectman, I. Blech, D. Gratias, J. W. Cahn, *Phys. Rev. Lett.* **53**, 1951 (1984).
14. N. D. Mermin and S. M. Troian, *ibid.* **54**, 1525 (1985).
15. P. A. Kalugin, A. Yu. Kitaev, L. S. Levitov, *JETP Lett.* **41**, 145 (1985).
16. S. Meiboom, J. P. Sethna, P. W. Anderson, W. F. Brinkman, *Phys. Rev. Lett.* **46**, 1216 (1981).
17. J. P. Sethna, *Phys. Rev. B* **31**, 6278 (1985).
18. M. J. Costello, S. Meiboom, M. J. Sammon, *Phys. Rev. A* **29**, 2957 (1984).
19. J. A. N. Zasadzinski, S. Meiboom, M. J. Sammon, D. W. Berreman, *Phys. Rev. Lett.* **57**, 364 (1986).
20. D. W. Berreman, J. A. N. Zasadzinski, M. J. Sammon, S. Meiboom, *ibid.*, p. 1737.
21. M. J. Sammon, J. A. N. Zasadzinski, M. Kuzma, *ibid.*, p. 2834.
22. J. A. N. Zasadzinski, *J. Phys.* (*Paris*) **51**, 747 (1990).
23. ______ and S. M. Bailey, *J. Electron. Microsc. Tech.* **13**, 309 (1989).
24. J. Patel, T. M. Leslie, J. W. Goodby, *Ferroelectrics* **57**, 137 (1984).
25. K. J. Ihn and J. A. N. Zasadzinski, in preparation.
26. M. Kléman, *Points, Lines, and Walls* (Wiley, Chichester, England, 1983), chap. 5.
27. D. L. Misell, in *Image Analysis, Enhancement and Interpretation*, vol. 7 of *Practical Methods in Electron Microscopy*, A. M. Glauert, Ed. (North-Holland, Amsterdam, 1978), chap. 4.
28. We thank J. Patel for suggestions on orienting the smectic samples. K.J.I. and J.A.N.Z. acknowledge financial support from the Whitaker Foundation Biomedical Engineering grant, the Donors of the Petroleum Research Fund, and the National Science Foundation under grants CBT86-57444 and CTS90-15537.

5 May 1992; accepted 20 July 1992

Microbial Control of Silicate Weathering in Organic-Rich Ground Water

Franz K. Hiebert and Philip C. Bennett

An in situ microcosm study of the influence of surface-adhering bacteria on silicate diagenesis in a shallow petroleum-contaminated aquifer showed that minerals were colonized by indigenous bacteria and chemically weathered at a rate faster than theoretically predicted. Feldspar and quartz fragments were placed in anoxic, organic-rich ground water, left for 14 months, recovered, and compared to unreacted controls with scanning electron microscopy. Ground-water geochemistry was characterized before and after the experiment. Localized mineral etching probably occurred in a reaction zone at the bacteria-mineral interface where high concentrations of organic acids, formed by bacteria during metabolism of hydrocarbon, selectively mobilized silica and aluminum from the mineral surface.

Chemical weathering of rock-forming silicate minerals at the Earth's surface is a fundamental process and is a basis of the global geochemical cycling of the elements (*1*). Silicate solubility and aqueous dissolution kinetics are reasonably well characterized and are known to be controlled by many variables, including crystal lattice defects, solution pH, temperature, ionic strength, and the presence or absence of inorganic and organic ligands (*2*). The role of microbes is rarely factored into models of subsurface rock-water interactions, even though silicates dissolve faster in microbially active organic-rich waters than predicted by estimates made on the basis of the bulk ground-water geochemical environment (*3*, *4*).

In the pH range of most natural waters, silicate dissolution is extremely slow (*2*). In the absence of complexing ligands, silica (SiO_2) is released from microcline at pH 7 and at 25°C at a rate of about $10^{-15.5}$ mol cm^{-2} s^{-1}. Under similar conditions, quartz dissolves at a rate of $10^{-16.5}$ mol cm^{-2} s^{-1} (*5*, *6*). Organic electrolytes, especially organic acids, accelerate the dissolution of feldspar at mildly acidic pH by surface complexing of metals that speed the breakdown of framework metal-oxygen bonds, which is considered the rate-limiting step

---

Department of Geological Sciences, The University of Texas at Austin, Austin, TX 79713.

(5). A few multifunctional organic acids accelerate quartz dissolution at near-neutral pH but only at high concentrations (6). These observations suggest that quartz and feldspar solubilities are controlled primarily by conventional inorganic equilibrium in ground water at near-neutral pH except under conditions of high concentrations of chelating organic acids.

Microbial metabolism of hydrocarbon, a common form of organic carbon in subsurface sedimentary systems, results in the production of a variety of metastable intermediate by-products, including organic acids (7). Depending on the geochemical environment, these by-products may build up to measurable quantities in the extracellular environment (8); however, little work has been done on defining the role that bacteria may play in influencing the fate of the surrounding rocks (9).

We examined the in situ rate of feldspar and quartz dissolution and the morphology of crystal surfaces weathered for 14 months in a microbially active, oil-contaminated ground water and documented the ground-water geochemistry over a 40-m flow path in the microbially active zone. The site of this experiment is a petroleum-contaminated sand and gravel aquifer near Bemidji, Minnesota (Fig. 1). Ground-water chemistry has been monitored since 1983 by the U.S. Geological Survey (3, 10).

Earlier work at the Bemidji location showed that indigenous microfauna utilize petroleum, produce organic acids as metabolic by-products, and alter the ground-water geochemistry (8). Seven common genera of aerobic bacteria known to utilize hydrocarbon have been identified and include *Acinetobacter, Aeromonas, Vibrio, Pseudomonas, Mycobacterium, Micrococcus,* and *Achromobacter* (11). Under the floating pool of oil, oxygen is consumed, and the ground water has a near-neutral pH. In this zone, SiO_2 is mobilized, probably from silicates, and the waters approach equilibrium with amorphous SiO_2. Native silicate sand grains collected from the contaminated zone are weathered, and evidence of chemical etching of quartz grains has been previously reported (3, 4, 10). It was impossible, however, to determine when the alteration occurred, how fast it proceeded, or the mechanism of apparently enhanced dissolution.

In order to examine possible mechanisms of silicate dissolution, we used in situ microcosm experiments and calculated field SiO_2 release rates. Crystals of albite, anorthite, anorthoclase, microcline, and quartz were crushed, dry-sieved to collect the 5- to 10-mm size fraction, and rinsed in distilled water (12). Crystal surfaces were cleaned of rock dust by brief low-power ultrasonification. Split samples of each prepared mineral type were characterized by scanning electron microscopy (SEM) and energy dispersive analysis by x-ray (EDAX) and reserved as reference and controls. The surface area of the experimental and aquifer material was estimated by geometric analysis and measured by both nitrogen and krypton Brunauer-Emmett-Teller (BET) sorption methods.

The remaining samples of crystal fragments were mixed and loaded into porous polyethylene cylinders (microcosms) and submerged in the aquifer for 14 months (13). The study wells were screened in ground water just below the floating pool of oil. The microcosms were suspended in the screened portion of the well about 10 cm below the oil layer. The well bore was purged with nitrogen, sealed, and left undisturbed for the duration of the experiment. Ground-water samples were collected during microcosm emplacement and recovery.

On recovery, microcosms were placed in sterile jars filled with formation water and stored at 4°C until analysis. Microcosm materials were split into archive and study portions and treated to fix biological tissue. Mineral grains were prepared for SEM inspection by critical-point drying and gold coating (14).

Aquifer sediments consist primarily of quartz (60%), mixed feldspars (30%), and some calcite and dolomite (5% total) (3, 10). The surface area of the bulk sediments is 1.8 m^2 g^{-1}. Water flowing under the oil pool is reducing, slightly acidic, has no detectable oxygen, and contains a high concentration of dissolved organic carbon (Table 1). The carbon is a combination of unaltered volatile petroleum components and partially degraded petroleum in the form of simple and complex organic acids (3, 8, 10).

Dissolved SiO_2 increases along the flow path from a background concentration of 0.2 mmol $liter^{-1}$ to a maximum of about

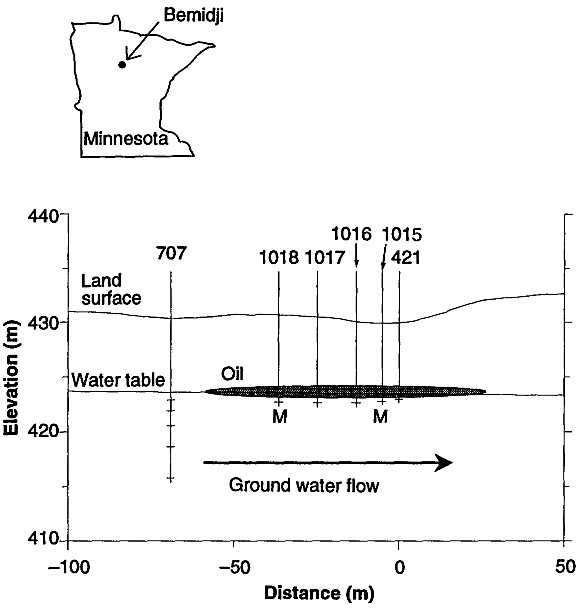

Fig. 1. Research site and cross section of aquifer flow path. Microcosms (M) were located in wells 1018 and 1015 as indicated. Crosses (+) indicate the location of well screens. The geochemistry of this aquifer has been studied for 10 years.

Table 1. Geochemical parameters of the aquifer flow path within which the experimental microcosms were placed. Although the values reported here represent the chemistry at a single point in time, there was little variation over the previous 4 years; thus, values in Table 1 probably represent a characteristic geochemistry.

Parameter	Well				
	707	1018	1017	1016	1015
Distance (m)*	0	36	47	58	70
pH	6.8	6.7	6.4	6.2	6.3
Si (ppm)	9.4	21.1	20.1	24.4	30.3
Al (ppb)	20	38	34	45	50
Ca (ppm)	142.2	168.7	163.8	170.7	164.3
Fe (ppm)	0	24.9	14.7	62.5	54.9
Dissolved inorganic carbon (ppm)	116	185	169	220	197
Dissolved organic carbon (ppm)	19	35	35	92	52

*Meters from edge of petroleum pool in aquifer.

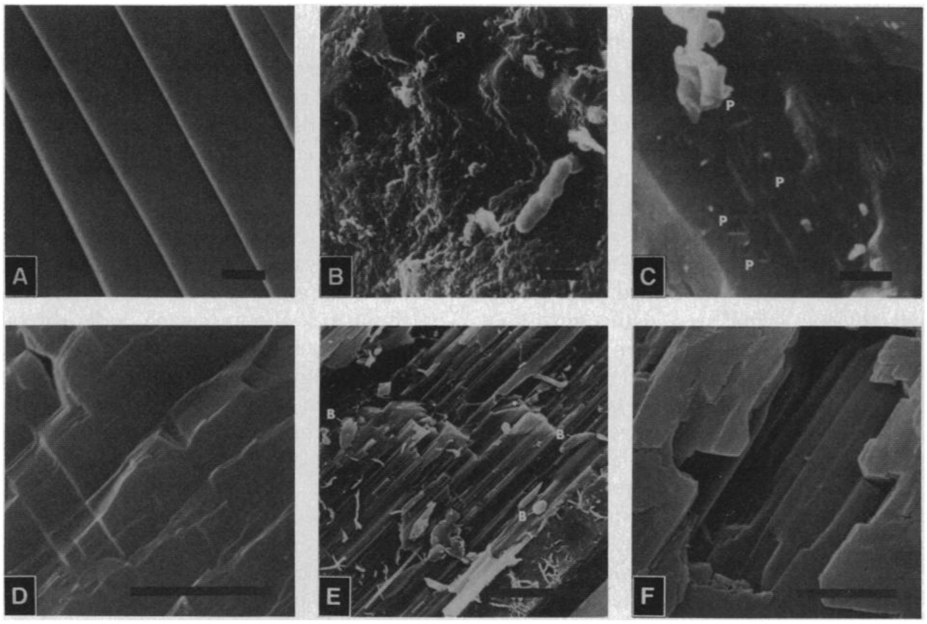

Fig. 2. Scanning electron micrographs of control and in situ–reacted mineral grains. (**A**) Surface of control quartz crystal shard. Note smooth surface and stair-step fracture pattern. Scale bar, 1 μm. (**B**) Surface of quartz crystal shard recovered from in situ microcosm after 14 months. Note triangular etch pits (P) on smooth surface and near bacteria. The bacterium in the central portion of the micrograph is dividing, indicating that bacterial growth occurs in the aquifer. Scale bar, 1 μm. (**C**) Etch pits (P) on the surface of quartz shard recovered from in situ microcosm after 14 months. The triangular morphology of the pits is characteristic of chemical etching; however, the chemistry of the bulk pore water indicates that dissolution of quartz should not have occurred. Scale bar, 1 μm. (**D**) Surface of control microcline crystal fragment. Smooth surfaces are evident between linear cleavage planes. Scale bar, 5 μm. (**E**) Surface of microcline crystal fragment recovered from in situ microcosm. Note deep chemical etching along the cleavage plane of the mineral. Bacteria (B) occur in three morphologies in the field of this micrograph. Dendritic fibrils are most likely clay minerals (kaolinite or halloysite). Scale bar, 5 μm. (**F**) Surface of microcline crystal fragment recovered from in situ microcosm. This crystal fragment was recovered from the same microcosm as that in (E) and has been ultrasonically cleaned of debris to reveal the deep chemical etching pattern on its surface. The morphology of these surface pits is similar to those produced in laboratory studies of chemical dissolution of feldspars (*6*). Scale bar, 5 μm.

1.0 mmol liter^{-1} under the center of the oil pool. The microcosms were located in ground water containing ~0.7 mmol liter^{-1} of dissolved Si where the change in dissolved SiO_2 with distance along the flow path is greatest (~10^{-12} mol m^{-2} s^{-1}, on the basis of 1.8 m^2 g^{-1} specific surface area, 3.5×10^{-6} m s^{-1} flow velocity, and a porosity of 30%). This dissolution rate is slightly greater than that expected for oligoclase, for example, at this temperature (*2*). If this rate were uniformly distributed over the entire exposed surface area, about 100 molecular layers would be removed, or about 0.1 μm of mineral surface over a 14-month period.

The amount of dissolved total Al is low, increasing from a background concentration of less than 1 to about 3 μmol liter^{-1}; most of the Al consists of monomeric hydroxy-Al or possibly organic-Al complexes. Although the increase in Al spatially corresponds to the increase in Si, the nearly 500:1 ratio of H_4SiO_4 to Al in a water where feldspar is dissolving suggests that Al is conserved in a solid phase. Calculations from chemical speciation and equilibrium models (*3*, *10*) show that the contaminated ground water is supersaturated with respect to quartz and approaches equilibrium with amorphous silica. The waters are supersaturated with respect to gibbsite and kaolinite but undersaturated with respect to the primary silicate phases such as anorthite, microcline, and albite, within the uncertainty of the thermodynamic database.

Examination of the reference mineral grains by SEM showed that the surfaces are clean and without evidence of chemical or mechanical weathering. Quartz grains are angular and irregular, and the surfaces consist of conchoidal and step fractures (Fig. 2A). Feldspar surfaces are smooth and irregular, and cleavage can be distinguished (Fig. 2D).

Examination of mineral surfaces from the microcosms, however, shows evidence of biological colonization and chemical alteration. Bacterial cells in a variety of morphologies colonized the mineral surfaces, primarily as individual cells and small patches (Fig. 2, B and E). Bacterial distribution was sparse, though ubiquitous, consistent with the results of previous studies of bacterial attachment to sediment in contact with hydrocarbon-rich fluids (*15*). We estimate that as much as 50% of the attached biomass may have dislodged during the critical-point drying, even though efforts were made to minimize sample disruption. Therefore, where we see individual cells and small colonies established on mineral grain surfaces, larger and more numerous colonies of bacteria may have been present.

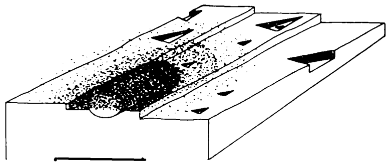

Fig. 3. Conceptual model of a bacterially generated microreaction zone at the surface of a quartz crystal fragment. Surface-adhering bacteria create a reaction zone in their immediate vicinity by producing and releasing organic acids during metabolism. The organic acids released by the cell create a gradient between the cell surface and the surrounding pore water. In this microenvironment, complex organic acids chelate SiO_2 from the mineral surface and cause dissolution despite the quartz-supersaturated status of the bulk pore water.

Intense chemical etching of feldspars and light but distinct etching of quartz was noted, especially in the vicinity of attached bacterial cells (Fig. 2, B, C, and E). Etching of quartz occurred in water that was many times supersaturated with respect to quartz (Table 1). Etching is seen as oriented triangular pits that are clearly grouped in discrete areas, whereas other areas are apparently unetched. An unknown solid phase precipitated on some mineral surfaces (Fig. 2B). The triangular etch pits noted on weathered quartz shards are diagnostic of crystallographic control of dissolution (*3*, *4*). The occurrence of these pits suggests that a volume of weathering fluid more reactive than ground water persisted at the mineral interface long enough to initiate etching. Etch pits in the shape of bacterial cells were not noted.

In contrast to the light weathering of quartz, some feldspar surfaces are locally intensely etched and weathered (Fig. 2, E and F). Etch pits are prismatic, varying from 1 to 5 μm in diameter, and are over 1 μm deep. The preferential orientation of prismatic etch pits along cleavage planes again suggests that dissolution was crystallographically controlled (*16*). During the 14-month period at 10°C, with the measured water composition, etching should have been on the order of 100 nm, in contrast to the deep localized weathering that actually occurred. Furthermore, the native feldspar grains collected from uncontaminated regions of the aquifer showed little evidence of chemical weathering, consistent with the expected inorganic dissolution rate (*10*).

Bacteria were located at or near the etch pits. The etch pits, however, are not at the actual contact surface of the microbes, and the distinctive shape and extent of etching suggest that the mineral surface is in contact with an aqueous weathering fluid. We postulate that surface-adhering bacteria created a reaction zone in their immediate vicinity in which organic acids, produced within the cell and released extracellularly, were concentrated at the cell solution–mineral interface (Fig. 3). During metabolism, organic substrate was consumed by heterotrophic bacteria, whereas enzymes and metabolic by-products such as organic acids were exported from the cell interior to the nearby fluid environment. A gradient in chemical potential was produced between the cell surface and the surrounding bulk fluid. High concentrations of these by-products may be present in the near vicinity of the microorganisms. Within this microenvironment, complex organic acids chelated SiO_2 at the quartz surface and dissolved the mineral even though the bulk pore water was supersaturated with respect to the dissolving mineral. Silica, and possibly alumina, thus chelated and in solution, is available for transport away from the dissolution site along the ground-water flow path.

The activity of indigenous microorganisms may represent a previously overlooked factor in modeling subsurface geochemistry. In addition, those geochemical processes reported may represent an alternative mechanism for the generation of secondary porosity in low-temperature (up to 70°C) sedimentary basins.

REFERENCES AND NOTES

1. E. K. Berner and R. A. Berner, *The Global Water Cycle, Geochemistry and Environment* (Prentice-Hall, Englewood Cliffs, NJ, 1987), pp. 148–165.
2. W. H. Huang and W. D. Keller, *Am. Mineral.* **55**, 2076 (1970); J. Schott, R. L. Berner, E. L. Sjoberg, *Geochim. Cosmochim. Acta* **45**, 2123 (1981); L. Chou and R. Wollast, *Am. J. Sci.* **285**, 963 (1985); G. R. Holdren and P. M. Speyer, *ibid.*, p. 994; K. G. Knauss and T. J. Wolery, *Geochim. Cosmochim. Acta* **50**, 2481 (1986); M. A. Mast and J. I. Drever, *ibid.* **51**, 2559 (1987).
3. P. C. Bennett, D. I. Siegel, *Nature* **326**, 684 (1987).
4. ______, B. M. Hill, P. H. Glaser, *Geology* **19**, 328 (1991).
5. W. Stumm and G. Furrer, in *Aquatic Surface Chemistry*, W. Stumm, Ed. (Wiley, New York, 1987), chap. 8.
6. P. C. Bennett, *Geochim. Cosmochim. Acta* **55**, 1781 (1991).
7. D. L. Balkwill and W. C. Ghiorse, *Appl. Environ. Microbiol.* **50**, 580 (1985); W. C. Ghiorse and J. T. Wilson, *Adv. Appl. Microbiol.* **33**, 107 (1988); E. L. Madsen, J. L. Sinclair, W. C. Ghiorse, *Science* **252**, 830 (1991); R. M. Atlas, Ed., *Petroleum Microbiology* (Macmillan, New York, 1984).
8. I. M. Cozzarelli, R. P. Eganhouse, M. J. Baedecker, *Environ. Geol. Water Sci.* **16**, 135 (1990).
9. Exceptions include F. H. Chapelle and D. R. Lovley, *Appl. Environ. Microbiol.* **56**, 1865 (1990); F. H. Chapelle and P. B. McMahon, *J. Hydrol.* **127**, 85 (1991); P. B. McMahon and F. H. Chapelle, *Nature* **349**, 233 (1991); ______, W. F. Falls, P. M. Bradley, *J. Sediment. Petrol.* **62**, 1 (1992).
10. M. J. Baedacker, D. I. Siegal, P. C. Bennett, I. M. Cozzarelli, *U.S. Geol. Surv. Water Res. Invest. Rep. 88-4220* (1989); M. J. Baedecker, I. M. Cozzarelli, P. C. Bennett, D. I. Siegel, in preparation.
11. F. H. Chang and G. Ehrlich, *U.S. Geol. Surv. Water Res. Invest. Rep. 84-4188* (1984).
12. Minerals were obtained from Wards Natural Science Establishment, Inc., albite 46E0230, -2 and -4; quartz 46E6605, -7 and -9; anorthite 46E0555, -7 and -9; and anorthoclase 46E0575, -7 and -9.
13. During the preparation of the mineral materials for these experiments, not all phases were carried out under strictly sterile conditions. However, standard techniques for the aseptic handling of microbial cultures and of sterile materials were used, and every effort was made to minimize the possibility of contamination of the mineral specimens by opportunistic microorganisms. Examination of mineral grains reserved as controls has not shown any evidence of microbial contamination.
14. J. W. Costerton, in *Adsorption of Microorganisms to Surfaces*, G. Bitton and K. C. Marshall, Eds. (Wiley, New York, 1980), chap. 12.
15. F. K. Hiebert, R. L. Folk, P. C. Bennett, C. H. Oppenheimer, L. W. Lake, *Eos* **71**, 503 (1990).
16. R. A. Berner and G. R. Holdren, Jr., *Geochim. Cosmochim. Acta* **43**, 1173 (1979); ______, J. Schott, *ibid.* **49**, 1657 (1985).
17. We thank R. L. Folk, M. J. Baedecker, I. M. Cozzarelli, D. I. Siegel, L. Crossey, and J. Horowitz. Supported by the National Science Foundation, the U.S. Geological Survey, and the Geology Foundation of The University of Texas at Austin.

20 May 1992; accepted 4 August 1992

Fault Zone Connectivity: Slip Rates on Faults in the San Francisco Bay Area, California

Roger Bilham and Paul Bodin

The slip rate of a fault segment is related to the length of the fault zone of which it is part. In turn, the slip rate of a fault zone is related to its connectivity with adjoining or contiguous fault zones. The observed variation in slip rate on fault segments in the San Francisco Bay area in California is consistent with connectivity between the Hayward, Calaveras, and San Andreas fault zones. Slip rates on the southern Hayward fault taper northward from a maximum of more than 10 millimeters per year and are sensitive to the active length of the Maacama fault.

The mean recurrence interval between damaging earthquakes on a fault is determined in part by its slip rate (*1*). Slip rate data are obtained by summing the moments of historic earthquakes (*2*) or by direct observation of the offset rate of geological features (*3*). Historic summations of seismic moment are inaccurate where the instrumental or written record endures for fewer than several earthquake cycles, as in California. Moreover, exhumation of faults to learn their historic slip rates can result in inaccurate estimates of slip rate at seismogenic depths because slip may be distributed over a wide region. For example, no surface evidence for fault slip exists for the inferred 1.8 m of dextral slip that accompanied the 1989 Loma Prieta earthquake (*4*), and slip on the nearby San Andreas fault during the 1906 San Francisco earthquake was significantly underestimated by observed fault offsets (*5*). Relative plate motion between the Pacific and North American plates is distributed principally among faults of the San Andreas system, a branching network of interconnected fault zones (*6*). Although detailed geodetic studies show the distribution of velocities across the plate boundary, these data do not contribute to our understanding of long-term slip rates on mapped faults. The observed deformation field may be generated by several plausible but non-unique distributions of slip on faults in the plate boundary (*7*). In this report we examine an alternative method to estimate the relative slip rates of faults in a complex plate boundary based on the geometry and mechanical linkage of mapped faults. In our proposed model we assume that the long-term slip rates of faults are determined by their current and evolving geometries.

For a wide range of fault lengths, the total geologic offset of a fault zone increases with fault zone length (*8*). Total offset is a maximum near the center of the fault zone and decays to small values near its ends. Similarly, the coseismic slip on an individual rupture increases with rupture length (*9*) and decays to zero at the ends of the rupture. Slip amplitude and distribution are influenced by the strain at failure (*10*), the geometry of the fault (*11, 12*), and the aspect ratio of the rupture surface (*13*). Earthquakes seldom rupture an entire fault zone. Instead they rupture segments or groups of segments that together result in the observed total offset of faults (*14*). As a result (Fig. 1), the slip rate of a segmented

---

Cooperative Institute for Research in the Environmental Sciences and Department of Geological Sciences, University of Colorado, Boulder, CO 80309–0216.